

Article

UBathy: A New Approach For Bathymetric Inversion From Video Imagery

Gonzalo Simarro ^{1,*}, Daniel Calvete ², Pau Luque ^{2,†}, Alejandro Orfila ³ and Francesca Ribas ²

¹ ICM (CSIC), Passeig Marítim de la Barceloneta 37-49, 08003 Barcelona, Spain

² Universitat Politècnica de Catalunya, Jordi Girona 1-3, 08034 Barcelona, Spain

³ IMEDEA (UIB-CSIC), Carrer Miquel Marqués 21, 07190 Esporles, Spain

* Correspondence: simarro@icm.csic.es

† Current address: SOCIB, Parc Bit, 07121 Palma de Mallorca, Spain

‡ These authors contributed equally to this work.

Version November 15, 2019 submitted to Remote Sens.

Abstract: A new approach to infer the bathymetry from coastal video monitoring systems is presented. The methodology uses Principal Component Analysis of the Hilbert transform of video images to obtain the components of the wave propagation field and their corresponding frequency and wavenumber. Incident and reflected constituents and subharmonics components are also found. Local water depth is then successfully estimated through wave dispersion relationship. The method is first applied to monochromatic and polychromatic synthetic wave trains propagated using linear wave theory over an alongshore uniform bathymetry, in order to analyze the influence of different parameters on the results. To assess the ability of the approach to infer the bathymetry under more realistic conditions, and to explore the influence of other parameters, nonlinear wave propagation is also performed using a fully nonlinear Boussinesq-type model over a complex bathymetry. In the synthetic cases, the relative root-mean-square error obtained in bathymetry recovery (for water depths $0.75 \text{ m} \leq h \leq 8.0 \text{ m}$) ranges from $\sim 1\%$ to $\sim 3\%$ for infinitesimal-amplitude wave cases (monochromatic or polychromatic) to $\sim 15\%$ in the most complex case (nonlinear polychromatic waves). Finally, the new methodology is satisfactorily validated through a real field site video.

Keywords: Video monitoring; Bathymetry inversion; Principal Component Analysis.

1. Introduction

Decision making in coastal zone management requires a knowledge of the bathymetry [1,2]. Obtaining accurate bathymetries has interest on its own, since it allows, e.g., to know how the waves propagate to the shore, how the morphology has evolved in time (if several bathymetries are available), or to decide if it is necessary to dredge the mouth of a harbour. Measuring bathymetric time-series also allows to validate morphodynamic numerical models, especially if obtained with a relatively high frequency. The morphodynamic models, in turn, can be a helpful tool to predict future changes and analyze the impact of potential human actions [3,4]. There is, consequently, a large interest in obtaining accurate bathymetries [5,6, to mention just a few].

In situ bathymetric measurement techniques include a wide variety of approaches that range from swath-sounding sonar systems [7] to bottom-contacting vehicles such as the Coastal Research Amphibious Buggy (CRAB) [5]. While *in situ* techniques provide excellent bathymetries at high spatial resolution, they are both expensive and highly time consuming. Except during experimental field campaigns, they are usually obtained at most few times per year. Alternatives to *in situ* methods include, among other, LiDAR techniques [8,9], satellite images [6,10], video images [11,12] and X-band

31 radar images [13,14]. The reader is referred to the work by [15] for a review. One technique will be
32 preferable relative to the others depending on aspects such as the size of the area to be analyzed or
33 the desired spatial and temporal resolution. For instance, satellite information is unbeatable for large
34 domains but it has a low spatial resolution and a limited temporal resolution. On the other hand, video
35 monitoring systems, the object of this work, provide excellent spatio-temporal resolution for domains
36 up to a few kilometers.

37 Video monitoring systems [16–18], mainly developed after the relatively recent advent of digital
38 cameras, have shown to be a powerful and low-cost tool to monitor the coast. These systems are
39 useful in a wide range of studies, such as, for example, shoreline detection and coastal variability
40 [2,19,20], intertidal bathymetry [21,22] or the study of the morphodynamics of beach systems [23–26].
41 Video systems have also shown to be able to give estimates of the bathymetry through the wave
42 propagation linear dispersion relationship, which relates the water depth to the wavenumber and
43 the wave frequency. For this purpose, the wave frequency and (space-varying) wavenumber are to
44 be obtained from a sequence of snap images. [11] obtained the wavenumber from the wave speed
45 (and the wave frequency) which, in turn, were obtained from timestack images of several transects
46 normal and parallel to the coast. From then on, there has been a considerable effort to develop reliable
47 techniques to obtain the bathymetry from video images, working both in 1D in space, i.e., in transects,
48 or treating the whole images, i.e., 2D [e.g.: 12,27]. Some of the proposed approaches use video images
49 combined with numerical models and/or radar images. Of mention, there have also been attempts to
50 obtain the bathymetry without the dispersion equation, using the wave dissipation pattern observed
51 in time averaged (*timex*) images instead of a sequence of snaps [28].

52 The cBathy algorithm [12] is nowadays the most popular algorithm to obtain 2D bathymetries
53 from video stations [e.g.: 29,30]. The code is made-up of two main parts: first, a bathymetry estimate
54 is obtained for each hourly video (typically of few minutes at ~ 0.5 Hz); second, given a bunch of
55 hourly (estimated) bathymetries, they are smoothed through a Kalman filter [31] to obtain the final
56 hourly estimates. In regard to the first part (i.e., the estimate of the bathymetry from one video, which
57 is the topic this work is focused on), cBathy first transforms each pixel intensity time history to the
58 frequency domain. To obtain the water depth at any given point, it then considers a neighborhood
59 of the point and obtains the wave spatial pattern through frequency-domain empirical orthogonal
60 functions of the Cross Spectral Matrices (CSMs) averaged within frequency bands of interest. The
61 latter is done to handle with the noisy data such as the video images. The analysis of the set of CSMs
62 allows to get the dominant frequencies (those whose signal are more *coherent*) and their corresponding
63 wavenumbers. The dispersion relationship then allows to obtain estimates of the local water depth for
64 each dominant frequency and a weighted average of them. Some limitations and/or known problems
65 of cBathy have been reported in the literature [30,32] (e.g., dealing with high wave heights, wet/dry
66 tiles or long waves).

67 In this work we propose an alternative to cBathy to obtain nearshore bathymetries from videos,
68 which is based on Principal Component Analysis (PCA) of the Hilbert transform of the video images.
69 This methodology consists on retrieving wave patterns from time-space complex-PCA analysis of video
70 images, i.e., avoiding the frequency-domain analysis, to subsequently obtain nearshore bathymetries.
71 The use of PCA in wave propagation problem was actually introduced prior to the popularization of
72 video monitoring stations [33]; in this work PCA was applied to data recorded through tide gauges
73 and the goal was detecting infragravity waves. The problems observed in that work (*a note of caution*,
74 actually), were related to the fact that the distance between the gauges was relatively large compared
75 to the wavelength. This is actually not expected to be a problem for video images detecting wind
76 waves, for the pixel size, projected in the space, is much smaller than the wavelength in the area of
77 interest. The presented algorithm, uBathy, takes its name from cBathy, but with “u” referring to ULISES
78 [34], the software it has been developed in.

79 The aim of the present contribution is to demonstrate the validity of this new methodology and
80 to find the algorithms and parameter values that optimize the result. In order to fully control the

81 conditions, most tests are performed with synthetic bathymetries and waves. To test the performance of
 82 uBathy in real conditions, the bathymetry inferred from a video captured in a field site is also included.
 83 The proposed methodology is first presented and illustrated with a simple 1D case (Section 2). The
 84 validity of the proposed approach is analyzed through synthetic wave fields, both linear and nonlinear,
 85 propagating over two different bathymetries (Section 3). Special emphasis is devoted in the recovery of
 86 the wave frequency and the wavenumber from the PCA analysis of the video. The influence of the most
 87 relevant parameters is further discussed (Section 4), such as the temporal and spatial discretization
 88 of the video or the parameters that influence the post-process of the PCA to recover the bathymetry.
 89 Additionally, a video from a field site is analyzed with the presented methodology to estimate a
 90 real bathymetry. The result is compared with the one obtained from cBathy. To conclude, the most
 91 important findings are listed (Section 5).

92 2. Methodology

93 The present algorithm relies on PCA, which is briefly described in Section 2.1 for completeness.
 94 From this algebraic decomposition, the frequency and wavenumber of the different wave components
 95 are determined (Sections 2.2 and 2.3), and henceforth the bathymetry is obtained (Section 2.4). All the
 96 steps are illustrated with a simple 1D case (for ease of representation).

97 2.1. Principal Component Analysis

98 Consider any spatio-temporal real-valued function, $f(\mathbf{x}, t)$, discretized in space and time into
 99 a matrix \mathbf{X} so that $X_{mn} = f(\mathbf{x}_m, t_n)$, with $m = 1, \dots, M$ and $n = 1, \dots, N$. When working with real
 100 video images, \mathbf{x}_m will be the real-world coordinates corresponding to the image pixels, t_n the time
 101 of each snapshot and f , typically, the value of the pixel intensity for the snapshot. Each column of \mathbf{X}
 102 corresponds to a stacked “snapshot”, while each row is the time record at a given point.

103 Let \mathbf{Y} be the demeaned matrix, built up by subtracting to each column of \mathbf{X} the time average
 104 space-vector, i.e.,

$$\langle f \rangle_m = \frac{1}{N} \sum_{n=1}^N f(\mathbf{x}_m, t_n), \quad m = 1, \dots, M,$$

105 so that

$$Y_{mn} = X_{mn} - \langle f \rangle_m. \quad (1)$$

106 Considering M time-depending variables, one for each row of the matrix \mathbf{Y} , their covariance matrix
 107 is $\mathbf{Y} \cdot \mathbf{Y}^T / N$. Singular value decomposition, key in PCA, allows to rewrite $\mathbf{Y} \in \mathcal{M}_{M \times N}$ (i.e., a $M \times N$
 108 matrix) as

$$\mathbf{Y} = \mathbf{U} \cdot \mathbf{S} \cdot \mathbf{V}^T, \quad (2)$$

109 with $\mathbf{U} \in \mathcal{M}_{M \times Q}$, $\mathbf{S} \in \mathcal{M}_{Q \times Q}$, $\mathbf{V} \in \mathcal{M}_{N \times Q}$ and $Q = \min\{M, N\}$. Further, $\mathbf{U}^T \cdot \mathbf{U} = \mathbf{V}^T \cdot \mathbf{V} = \mathbf{I}_{Q \times Q}$,
 110 the identity, and \mathbf{S} is a diagonal matrix of real positive values (by convention, in decreasing order
 111 in the diagonal). Following usual notation, the q -th column of \mathbf{U} , a spatial vector, is the “Empirical
 112 Orthogonal Function” EOF_q , while the q -th row of the product $\mathbf{S} \cdot \mathbf{V}^T$, a time vector, is the “Principal
 113 Component” PC_q . From equations (1) and (2),

$$X_{mn} = \langle f \rangle_m + \sum_{q=1}^Q \text{EOF}_q(\mathbf{x}_m) \text{PC}_q(t_n). \quad (3)$$

114 The EOFs (columns of \mathbf{U}) are a set of orthonormal vectors in space, while the PCs (rows of $\mathbf{S} \cdot \mathbf{V}^T$)
 115 are a set of orthogonal vectors in time. Each pair $\{\text{EOF}_q, \text{PC}_q\}$ is a *mode* of the decomposition. The PCs

116 can be interpreted as a rewritten version of the information in \mathbf{Y} using the EOFs as a basis in equation
117 (2). The covariance matrix of the data expressed in this new basis is

$$\frac{1}{N} (\mathbf{S} \cdot \mathbf{V}^T) \cdot (\mathbf{S} \cdot \mathbf{V}^T)^T = \frac{1}{N} \mathbf{S} \cdot \mathbf{S}^T,$$

118 i.e., a diagonal matrix. The contribution of each PC_q and the corresponding EOF $_q$ to the total signal is
119 quantified by the values of the diagonal matrix $\mathbf{S} \cdot \mathbf{S}^T$, which indeed represents the explained variance,
120 $\sigma_q^2 = (\mathbf{S} \cdot \mathbf{S}^T)_{qq}$. For complex-valued signals, the above results hold as long as transposed matrices are
121 substituted by conjugate-transposed matrices. In that case both EOF $_q$ and PC_q become complex-valued
122 vectors, but σ_q^2 remains real-valued.

123 Propagation of small-amplitude waves over a flat bed can be described as [35]

$$f = \sum_{j=1}^J a_j \cos (\mathbf{k}_j \cdot \mathbf{x} - \omega_j t + \varphi_j),$$

124 where J is number of components of the wave field, a_j are the amplitudes, $\mathbf{k}_j = (k_{xj}, k_{yj})$ are the wave
125 vectors (with corresponding wavenumbers $k_j = |\mathbf{k}_j|$), $\omega_j = 2\pi/T_j$ are the angular frequencies (with
126 T_j being the wave periods) and φ_j are the wave phase lags. The time-wise Hilbert transform is

$$\mathcal{F} = \sum_{j=1}^J a_j \exp (-i (\mathbf{k}_j \cdot \mathbf{x} + \varphi_j)) \exp (i \omega_j t), \quad (4)$$

127 and the corresponding space and time discretized matrix reads

$$X_{mn} = \sum_{j=1}^J a_j \exp (-i (\mathbf{k}_j \cdot \mathbf{x}_m + \varphi_j)) \exp (i \omega_j t_n). \quad (5)$$

128 For large time domains it is $\langle f \rangle_m \sim 0$ and $Y_{mn} \sim X_{mn}$. The J time-wise complex vectors, i.e.,
129 $\exp (i \omega_j t_n)$, tend to be orthonormal as also the space-wise vectors do, i.e. $\exp (-i (\mathbf{k}_j \cdot \mathbf{x}_m + \varphi_j))$, and
130 the equation (5) is already the PCA decomposition of the signal into its monochromatic components
131 (with ω_j and \mathbf{k}_j). In this case, the explained variance for the q -th mode reads

$$\sigma_q^2 = \frac{a_q^2}{\sum_{j=1}^J a_j^2}. \quad (6)$$

132 Hence, each component of the wave field can be linked to a mode of the PCA. Moreover, the angle
133 of a given PC and EOF can be used to obtain the ω_j and k_j , respectively, of the corresponding wave
134 component since

$$\alpha_t = \text{angle} \{ \text{PC} (t) \} \approx \text{angle} \{ \exp (i \omega_j t) \} = \omega_j t, \quad (7a)$$

$$\alpha_x = \text{angle} \{ \text{EOF} (\mathbf{x}) \} \approx \text{angle} \{ \exp (-i (\mathbf{k}_j \cdot \mathbf{x} + \varphi_j)) \} = - (\mathbf{k}_j \cdot \mathbf{x} + \varphi_j). \quad (7b)$$

135 Above we have considered $\mathbf{k}_j \cdot \mathbf{x}$, while in wave propagation over uneven beds \mathbf{k}_j is not constant and
136 the spatial phase $\varphi_j (\mathbf{x}) = \int \mathbf{k}_j \cdot d\mathbf{x}$ has to be used instead. As shown below, this will not actually be a
137 limitation.

138 The usefulness of PCA to analyze wave propagation over uneven beds (i.e., with variable k) is
139 illustrated with the *linear* 1D propagation of waves. The bathymetry considered is defined by a water
140 depth, h , equal to

$$h(x) = 6 \text{ m} - 4 \text{ m} \tanh \left(\frac{x - 100 \text{ m}}{20 \text{ m}} \right), \quad 0 \leq x \leq 200 \text{ m}. \quad (8)$$

141 To represent more realistic sea state situations at the coast, where waves with different frequencies
 142 and wavenumbers can coincide, the superposition of two wave trains has been considered. The free
 143 surface elevation η (waves travelling rightwards) is

$$\eta(x, t) = \sum_{j=1}^2 a_j(x) \cos(\phi_j(x) - \omega_j t + \varphi_j) .$$

144 The amplitudes, $a_j(x)$, are obtained from the amplitudes at $x = 0$, a_j^0 , using fundamentals of linear
 145 wave propagation theory [35]. The wavenumbers k_j are related to the angular frequencies and the
 146 water depth through the dispersion relationship

$$\omega_j^2 = gk_j \tanh(k_j h) .$$

147 Three synthetic linear wave propagation cases are considered (Table 1), including a case with only
 148 one wave train (monochromatic), a case with two wave trains of different frequencies (bi-chromatic)
 149 and a case with two wave trains of the same frequency but opposite propagation directions (reflective).
 150 This allows to describe different features of the PCA. The discretization considers $x_m = m\Delta x$ and $t_n =$
 151 $n\Delta t$, with $\Delta x = 1$ m, $m = 1, \dots, M = 200$ (so that $x_{\max} = 200$ m), $\Delta t = 0.25$ s, and $n = 1, \dots, N = 400$
 152 (so that $t_{\max} = 100$ s).

cases	T_1 [s]	a_1^0 [cm]	dir ₁	T_2 [s]	a_2^0 [cm]	dir ₂
monochromatic	5.1	3.0	+	—	—	—
bi-chromatic	5.1	3.0	+	8.3	1.0	+
reflective	5.1	3.0	+	5.1	1.0	—

Table 1. Wave conditions in the seaward boundary for the 1D examples. For each wave train (two at most): T_j is the period, a_j^0 is the wave amplitude at $x = 0$ and dir _{j} the direction of wave propagation (+, rightwards).

153 For the monochromatic case, the analysis of the signal yields one main mode that represents 99.5%
 154 of the variance (Table 2). For the bi-chromatic case, two main modes are obtained (corresponding to
 155 the two components), with variances $\sigma_1^2 = 87.6\%$ and $\sigma_2^2 = 12.1\%$ (i.e., that account for the 99.7% of
 156 the total variance). Finally, when two waves with the same period and moving in opposite directions
 157 are superimposed (reflective case), only one mode that represents 99.7% of the variance is obtained out
 158 of the PCA.

159 The angles of the PCs and EOFs of the three cases are represented in the top panels of Figures 1
 160 and 3 respectively. In the monochromatic case, the slope of the angle α_t of the PC, leaving aside
 161 the jumps from π to $-\pi$, is approximately constant. The slope of the angle α_x of the EOF is gentler
 162 at $x = 0$ than at $x = 200$ m and acknowledges the dependence of the wavenumber on the water
 163 depth. In the bi-chromatic case each mode corresponds to one of the superimposed waves: the
 164 slope of α_t is gentler for the second mode than for the first one, consistently with the fact that
 165 $\omega_2 = 0.757$ rad/s $<$ 1.232 rad/s $= \omega_1$. In the reflective case, where there is only one mode, α_t is similar
 166 to the monochromatic case but now α_x has a wavy behavior, resulting from the superposition of two
 167 waves with the same frequency.

168 2.2. Wave frequency and wavenumber: phase fitting

169 The wave angular frequency (just frequency hereafter) at a certain time t_0 is to be determined by
 170 fitting the angle of the PC in a vicinity of radius R_t around t_0 , making use of equation (7a). However,
 171 to prevent the discontinuities in α_t , the latter is first centered at t_0 ,

$$\hat{\alpha}_t = \text{angle} \{ \exp(i(\alpha_t - \alpha_t(t_0))) \} = \text{angle} \{ \text{PC}(t) \overline{\text{PC}}(t_0) \} , \quad (9)$$

	mode	σ^2 [%]	T [s]
monochromatic	1	99.5	5.1
by-chromatic	1	87.6	5.1
	2	12.1	8.3
reflective	1	99.7	5.1

Table 2. Summary of the results of the PCA obtained for the 1D examples.

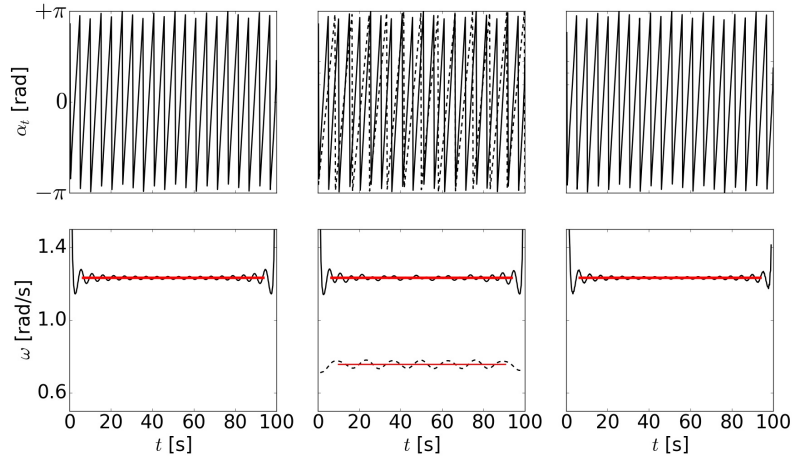


Figure 1. Angle of the PC (top), and frequency (bottom), for the monochromatic (left), bi-chromatic (center) and reflective (right) 1D cases, versus time. First (second) mode in solid (dashed) lines. Red lines for the mean angular frequencies.

172 where complex conjugated values are denoted with an overline. Figure 2 illustrates how $\hat{\alpha}_t$ avoids the
 173 discontinues for $t_0 = 10$ s and considering $\Delta t = 1$ s and $R_t = 3$ s. In a second step, being $\hat{t} = t - t_0$, $\hat{\alpha}$ is
 174 fitted through the expression

$$\hat{\alpha}_t \approx p_0 + p_1 \hat{t},$$

175 so that the frequency at t_0 is estimated as $\omega = p_1$. This fitting method will be referred to as *phase fitting*.
 176 An analogous phase fitting procedure can be applied to determine the wavenumber, k , from α_x in
 177 equation (7b).

178 Figure 1 (bottom panels) shows, in black, $\omega(t)$ obtained in the 1D examples, with $R_t = 0.5$ s
 179 ($\Delta t = 0.25$ s in the example). The observed overshoots in $\omega(t)$ at the domain boundaries are related to
 180 the discrete Hilbert transform. For each PCA mode, corresponding to a travelling wave, the frequency
 181 must be constant. This constant value is estimated by averaging $\omega(t)$, but skipping the values at a time
 182 distance of $\approx T$ near the boundaries. This averaged frequency will hereafter be referred to as ω and it
 183 is plotted in red in Figure 1. For the monochromatic and reflective cases $\omega \sim \omega_1 = 1.232$ rad/s (Table
 184 2, expressed as period), and for the bi-chromatic case the first mode gives $\omega \sim \omega_1$ and the second
 185 mode gives $\omega \sim \omega_2 = 0.757$ rad/s. In all cases the relative error in ω_1 and ω_2 is less than 0.05%. The
 186 standard deviation, σ_ω , of the values of $\omega(t)$ used to obtain ω can be regarded as a measure of the
 187 quality of the recovered frequency. Above, $\sigma_\omega/\omega < 1\%$ for the first modes and $\sigma_\omega/\omega \sim 2\%$ for the
 188 second mode in the bi-chromatic case.

189 Figure 3, second row, shows the values of k obtained in the 1D examples through phase fitting
 190 of α_x with $R_x = 2$ m ($= 2\Delta x$). The behavior of the wavenumber is smooth (with small oscillations),
 191 except for the reflective case (right), which is unrealistic but consistent with the corresponding α_x . In
 192 order to cope with reflected waves, which can occur in some real conditions, an alternative method to
 193 obtain k must be developed.

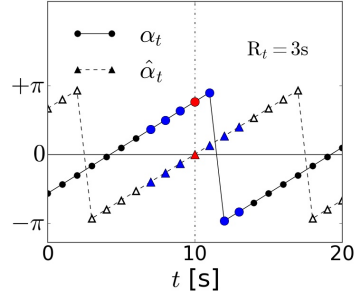


Figure 2. Angle of the PC before centering (circles) and after centering around $t = t_0 = 10$ s (triangles) for $\Delta t = 1$ s and $R_t = 3$ s. Red denotes the point of interest and blue indicates the neighbour points used.

194 2.3. Wavenumber: function fitting

195 If non-negligible reflection occurs, the EOF contains the information of both the incident and
196 reflected wave, i.e.

$$\text{EOF} \approx A_a \exp(-i(\mathbf{k}_a \cdot \mathbf{x} + \varphi_a)) + A_b \exp(-i(\mathbf{k}_b \cdot \mathbf{x} + \varphi_b)), \quad (10)$$

197 with the condition $|\mathbf{k}_a| = |\mathbf{k}_b| = k$. To obtain k and the rest of parameters involved, and following
198 the procedure described before for the frequency (section 2.2) but now including a normalization, we
199 first define

$$\widehat{\text{EOF}} = \frac{\text{EOF}(\mathbf{x}) \overline{\text{EOF}(\mathbf{x}_0)}}{|\text{EOF}(\mathbf{x}_0)|^2},$$

200 so that $\widehat{\text{EOF}}(\mathbf{x} = \mathbf{x}_0) = 1$ (real), with \mathbf{x}_0 being the point where the wavenumber is being estimated.
201 The expression (10) is then

$$\widehat{\text{EOF}} \approx \hat{A}_a \exp(-i(\mathbf{k}_a \cdot \hat{\mathbf{x}} + \hat{\varphi}_a)) + \hat{A}_b \exp(-i(\mathbf{k}_b \cdot \hat{\mathbf{x}} + \hat{\varphi}_b)), \quad (11)$$

202 where $\hat{\mathbf{x}} = \mathbf{x} - \mathbf{x}_0$. The function (11) is therefore fitted to the normalized EOF, by optimization, in the
203 neighborhood of $\mathbf{x} = \mathbf{x}_0$. The seven optimization parameters are $\hat{A}_a, \hat{A}_b, \hat{\varphi}_a, \hat{\varphi}_b, |\mathbf{k}_a| = |\mathbf{k}_b| = k$ and
204 the two angles (directions) of the wavenumbers. The wavenumbers obtained with this method match
205 the analytical values in all three cases of the 1D example (not shown). This method to get k , that will
206 be referred to as *function fitting*, is computationally much more expensive than phase fitting (around
207 two orders of magnitude).

208 2.4. Depth inversion

209 Once ω (constant) and k (space-varying) have been estimated, the local water depth, h , can be
210 inferred from the dispersion equation [12]. Being $\gamma = \omega^2/gk$, it reads

$$h = \frac{1}{k} \text{atanh}(\gamma). \quad (12)$$

211 Figure 3 (third and fourth rows) shows the results of h in the three 1D cases using, respectively,
212 phase fitting and function fitting approaches for k (ω is always computed with phase fitting). The exact
213 bathymetry of equation (8) is also included in the figure (blue lines). Most interestingly, the function
214 fitting method allows to properly recover the bathymetry in the reflective case, where the phase fitting
215 method fails. From Figure 3, for the non-reflective cases and for the first mode, the function fitting
216 method avoids the small oscillations observed in the phase fitting method. The function fitting can also

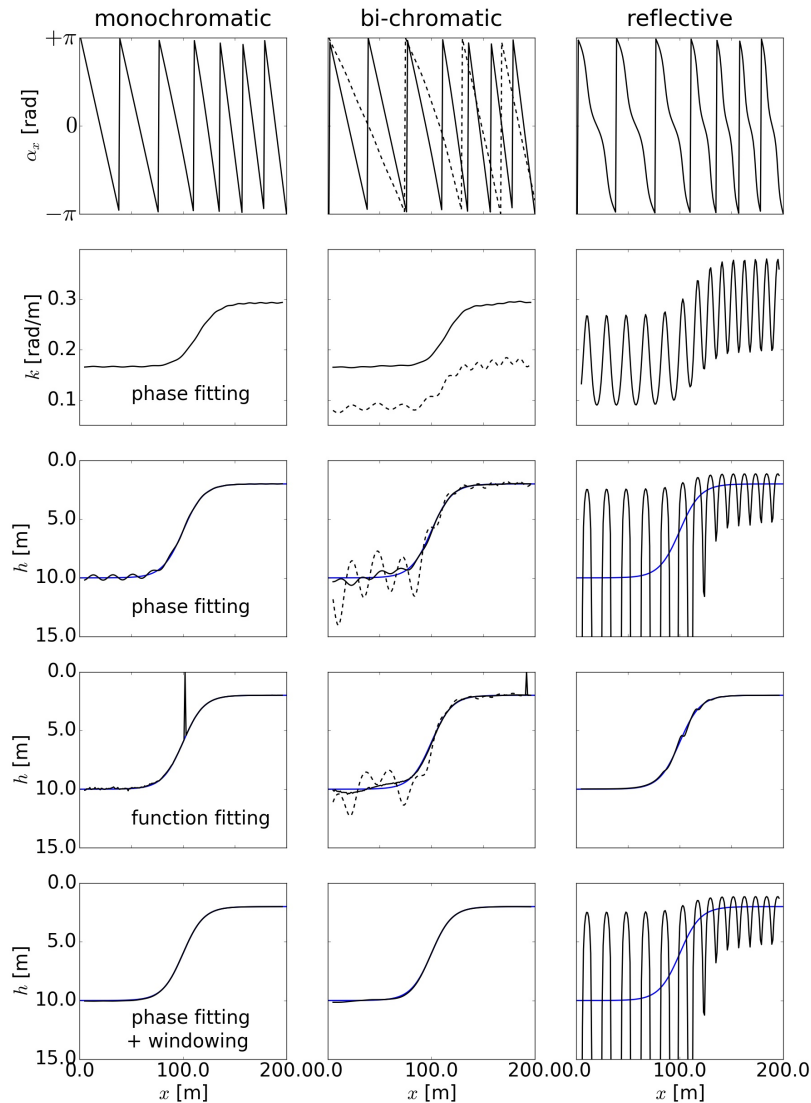


Figure 3. From top to bottom: angle of the EOF, wavenumber from phase fitting and depth from phase fitting, function fitting and windowing ($w_t = 40$ s). From left to right: monochromatic, bi-chromatic and reflective 1D cases. First (second) mode in solid (dashed) lines. Blue lines for the exact depth.

217 produce spurious peaks, which are due to the difficulties in the optimization to obtain the parameters
 218 in equation (10). This errors can be avoided by further increasing the computational time.

219 To reduce the errors associated to the small oscillations observed for the phase fitting method
 220 with a low computational cost, and to handle real videos that might include time intervals with large
 221 noise, an extension of the above scheme is proposed. First, instead of performing one unique PCA, all
 222 the sub-videos obtained from a moving time window of width w_t are analyzed, and only the dominant
 223 PCA mode of each sub-video is considered for the analysis. Second, for each time window, t_i , a
 224 pair $\{\omega_i, \sigma_{\omega_i}\}$ is obtained from the first PC, and sub-videos for which $\sigma_{\omega_i}/\omega_i > 15\%$ are discarded
 225 assuming that the recovered ω_i is not good enough. Third, for each time window k is obtained from
 226 the first EOF using the phase fitting method. Since the recovery of k might be unfeasible at some
 227 points, those points where the correlation coefficient of the fitted α_x are below 0.70 are filtered out
 228 as well. Finally, in a fourth step and following [12], the bathymetry at each point is the result of the
 229 best fit of the dispersion relationship (12) using all the pairs $\{\omega_i, k_i\}$ obtained in a neighborhood R'_x of
 230 the point ($R'_x = 0$ meaning that only the values at the point are considered). This extension will be

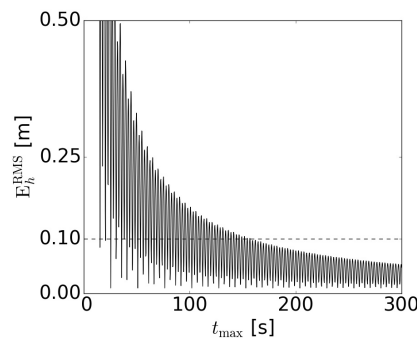


Figure 4. Evolution of the RMS error in h as a function of t_{\max} for the monochromatic case using phase fitting (without windowing).

referred to as *windowing* method. The last row in Figure 3 shows, for the same examples, the results of the windowing method with $w_t = 40$ s and $R'_x = 0$. While the reflective case cannot be recovered, as expected, it is seen how the recovered bathymetry fits the exact one in the monochromatic and bi-chromatic cases.

The oscillations, and related errors, observed using the phase fitting method can also be reduced by increasing the total time of the video (for non-reflective cases only). Following the above example, Figure 4 shows the evolution of the root mean square error of the obtained bathymetry, E_h^{RMS} , as a function of time t_{\max} using phase fitting (without windowing) for the monochromatic case. As a general trend, the error (from the oscillatory pattern in h) reduces as t_{\max} increases. The oscillatory behavior in Figure 4 is related to the time domain adjusting (or not) to a multiple of the wave period. For $t_{\max} = 300$ s the error is below 5.5 cm. In Figure 3, corresponding to $t_{\max} = 100$ s, the errors E_h^{RMS} for the monochromatic case are 10.5 cm (phase fitting), 4.3 cm (function fitting) and 2.8 cm (phase fitting + windowing).

3. Results

The proposed methodology introduces parameters such as the resolution of the spatio-temporal discretization (Δt and Δx), the radius (R_t and R_x) of the neighborhoods to recover the wave frequency and the wavenumber from the PCs and EOFs, the video duration (t_{\max} , assuming that the video starts at $t = 0$), or the parameters defining the windowing (w_t and R'_x). The influence of these parameters is studied using synthetic linear and nonlinear 2D wave fields. Linear wave propagation equations assume that the wave height is infinitesimally small and, for alongshore uniform bathymetries, simple analytical solutions can be computed. The synthetic linear wave fields will be used to analyze the influence of Δt , Δx , R_t and R_x . These linear solutions, however, dismiss wave reflections at the shore, and are unable to represent other important features of real wave fields such as wave decomposition (energy transfer from one frequency to other) or wave-wave interactions. For this reason, realistic non-linear numerical models are also used to examine other phenomena: propagation over complex bathymetries, generation of subharmonics and wave reflection. The synthetic nonlinear 2D wave fields will also allow to investigate the influence of t_{\max} and w_t (time windowing).

3.1. Analysis for synthetic linear waves: phase fitting

Three monochromatic wave trains (W1, W2 and W3, Table 3), and their superposition ($WS = W1 + W2 + W3$), are propagated over an alongshore uniform bathymetry (Figure 5, left). This bathymetry corresponds to a beach profile with a shore-parallel bar located 80 m from the shore. Wave conditions are meant to provide different wave periods in a realistic range and different propagation directions to check whether the obtained bathymetry is mainly independent of the wave characteristics. Notice that,

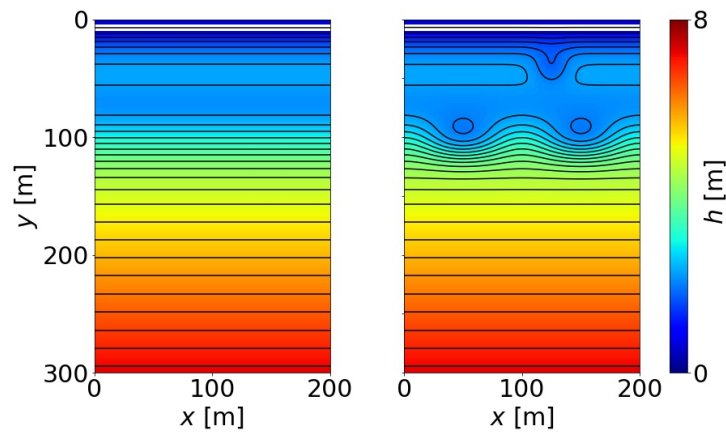


Figure 5. Bathymetries (in meters) for the analysis of linear waves (left) and nonlinear waves (right). The white strip next to the shore highlights $h = 0.75$ m.

wave train	T [s]	A [cm]	θ [°]	φ [°]
W1	7.945	10.0	-16.588	39.0
W2	12.00	6.0	+0.0	0.0
W3	5.022	2.0	+26.079	108.7

Table 3. Wave conditions in the seaward boundary for the analysis of synthetic 2D cases. For each wave train, T is the period, A is the wave amplitude in deep waters, θ is the angle with respect to the shore-normal in deep waters and φ is a phase lag.

264 since linear wave theory assumes infinitesimal amplitudes, in this section the amplitudes of Table 3
 265 are only to show the influence of the relative strength of the different wave trains in the WS case.

266 Knowing the wave conditions in the seaward boundary (Table 3), the waves are propagated
 267 towards the coast using the linear wave theory [35]. The initial snapshots for W1, W2, W3 and WS are
 268 shown in Figure 6. In all cases, the spatial domain is $200 \text{ m} \times 300 \text{ m}$ (in the alongshore and cross-shore
 269 directions, respectively) and the time domain is of 90 s. The video snapshots, X_{mn} , are obtained by
 270 assigning to each pixel an intensity that is a linear function of the free surface elevation.

271 In this section 3.1, only the phase fitting method is applied. Within this Section 3.1, windowing is
 272 not considered so as to focus on the influence of Δt , Δx , R_t and R_x . The influence of the spatio-temporal
 273 discretization (Δt and $\Delta x = \Delta y$) of the signal is analyzed considering all combinations of $\Delta x = \Delta y$ in

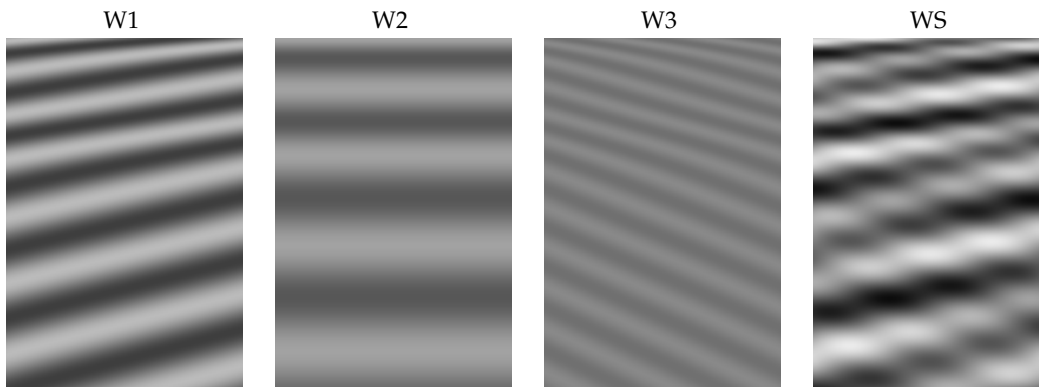


Figure 6. Initial snapshots for linear synthetic wave trains W1, W2 and W3 and their superposition WS. Spatial domain is $200 \text{ m} \times 300 \text{ m}$ (in the alongshore and cross-shore directions, respectively) and pixel intensity is a linear function of the modelled free surface elevation.

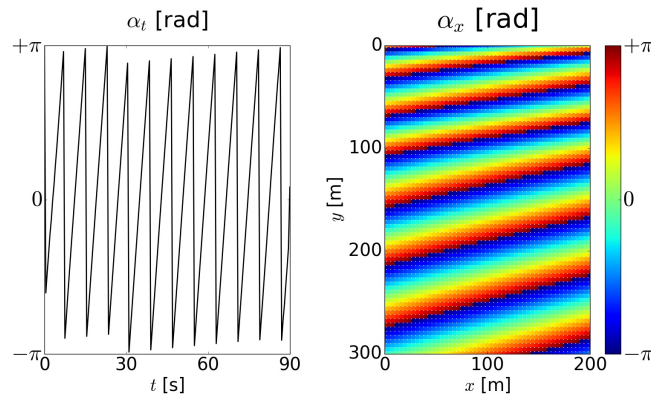


Figure 7. Angles α_t and α_x of the first PC and EOF corresponding to linear propagation of W1 for $\Delta t = 0.5$ s and $\Delta x = 4$ m. The explained variance is above 99%.

R_t [s]	Δt [s]			
	0.25	0.50	1.0	2.0
0.5	-0.066	-0.049	—	—
1.0	-0.101	-0.092	-0.051	—
2.0	-0.105	-0.105	-0.095	0.024
4.0	-24.7	-48.4	-72.7	-55.4

Table 4. Relative errors for ω , ϵ_ω (in %), as a function of Δt and R_t for $\Delta x = 2$ m, corresponding to linear propagation of W1.

274 {1 m, 2 m, 4 m, 10 m} and Δt in {0.25 s, 0.5 s, 1 s, 2 s, 4 s}. A major result of the PCA for monochromatic
 275 waves is to obtain one main mode that explains, in all cases, more than 98% of the total variance of the
 276 signal and that matches the corresponding wave train. The results found for the three monochromatic
 277 wave trains are qualitatively similar and the focus hereafter is on W1. For illustrative purposes, Figure 7
 278 shows an example of the angles α_t and α_x , capturing the refraction of the propagation as the wave
 279 train travels to the shore (compare α_x with W1 in Figure 6). For $\Delta t = 4$ s the PCA decomposition yields
 280 useless results for any Δx and hereafter results with $\Delta t = 4$ s have been disregarded.

281 The wave frequency from the PC has been computed for all the combinations of Δt and Δx and
 282 for different values of R_t in {0.5 s, 1.0 s, 2.0 s, 4.0 s}. The relative errors of the recovered ω , ϵ_ω , for W1
 283 are shown in Table 4 for $\Delta x = 2$ m. It turns out that results are independent of Δx . The case $R_t = 4$ s,
 284 giving large errors, is not considered in the following. The wavenumber k from the EOFs has been
 285 computed for the 2D-spatial domain using values of R_x in {2 m, 4 m, 8 m, 12 m, 16 m} and the different
 286 combinations of Δx and Δt . Figure 8 (top panels) shows an example of the recovered k as well as the
 287 local relative error, ϵ_k , obtained from the first (and *only*) EOF of the wave train W1. As depicted in
 288 the figure, ϵ_k is below $\sim 1\%$. The global relative RMSE, ϵ_k^{RMS} , obtained for the full set of exploration
 289 results is shown in Table 5 for the domain restricted to depths $h \geq 0.75$ m (see also Figure 5 where
 290 $h = 0.75$ m is highlighted). As occurred with Δx in the frequency recovery, the influence of Δt is minor
 291 when computing k (only $\Delta t = 0.5$ s is shown in Table 5).

292 Once ω and k are obtained from the only PCA mode of each monochromatic wave train, the
 293 corresponding bathymetry can be derived. Figure 8 (bottom panels) shows the bathymetry and the
 294 error obtained from the same case above. The inversion produces small errors, the largest errors being
 295 located in the shallower area. As in the 1D example, very small oscillations appear manifestly in k and
 296 especially in h . A summary of the results from the PCA for each monochromatic wave train and the
 297 corresponding global relative errors in ω , k and h is presented in Table 6 (upper half) for W1, W2 and
 298 W3. The errors in k and h are significantly larger for W3, which corresponds to the wave field with the
 299 smallest period.

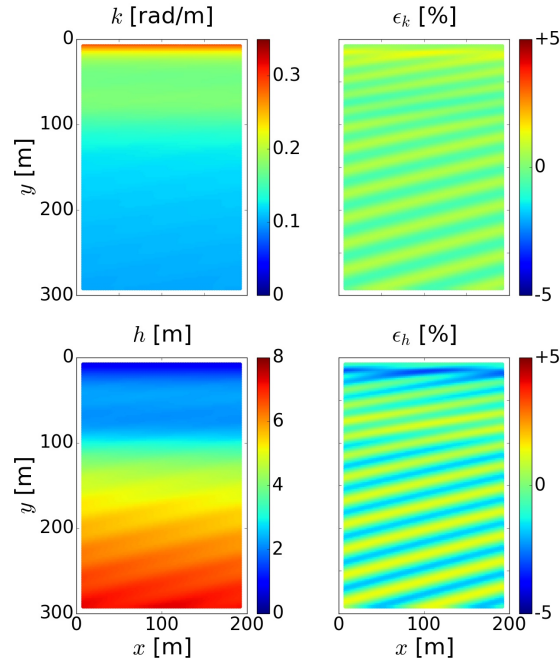


Figure 8. Recovered k (top, left) and h (bottom, left) and the corresponding local relative errors, ϵ_k and ϵ_h (right panels, in %), obtained using the phase fitting method for the first EOF corresponding to linear propagation of W1 and for $\Delta t = 0.5$ s, $\Delta x = 2$ m, $R_t = 1$ s and $R_x = 8$ m.

R_x [m]	Δx [m]			
	1	2	4	10
2	0.583	0.578	—	—
4	0.542	0.530	0.508	—
8	0.466	0.468	0.487	—
12	1.279	1.002	4.579	0.741
16	5.534	5.453	6.091	0.732

Table 5. Relative RMSE for k , ϵ_k^{RMS} (in %), for $h \geq 0.75$ m, as a function of Δx and R_x for $\Delta t = 0.5$ s and $R_t = 1.0$ s, corresponding to linear propagation of W1.

	mode	σ^2 [%]	T [s]	ϵ_ω [%]	ϵ_k^{RMS} [%]	ϵ_h^{RMS} [%]
monochromatic	1	99.2	7.952 [W1]	-0.092	0.468	1.083
	1	98.7	11.993 [W2]	0.062	0.526	1.085
	1	99.9	5.022 [W3]	-0.003	4.232	18.572
polychromatic	1	71.0	7.955 [W1]	-0.122	1.432	3.182
	2	25.3	11.949 [W2]	0.423	2.703	5.826
	3	2.9	5.028 [W3]	-0.124	6.665	27.554

Table 6. Summary of the results of the PCA obtained using phase fitting (without windowing) for linear wave propagation and $\Delta t = 0.5$ s, $\Delta x = 2.0$ m, $R_t = 1.0$ s, $R_x = 8$ m. Relative RMS errors, ϵ_k^{RMS} and ϵ_h^{RMS} , are given for $h \geq 0.75$ m. Next to the retrieved period, the corresponding wave field is indicated.

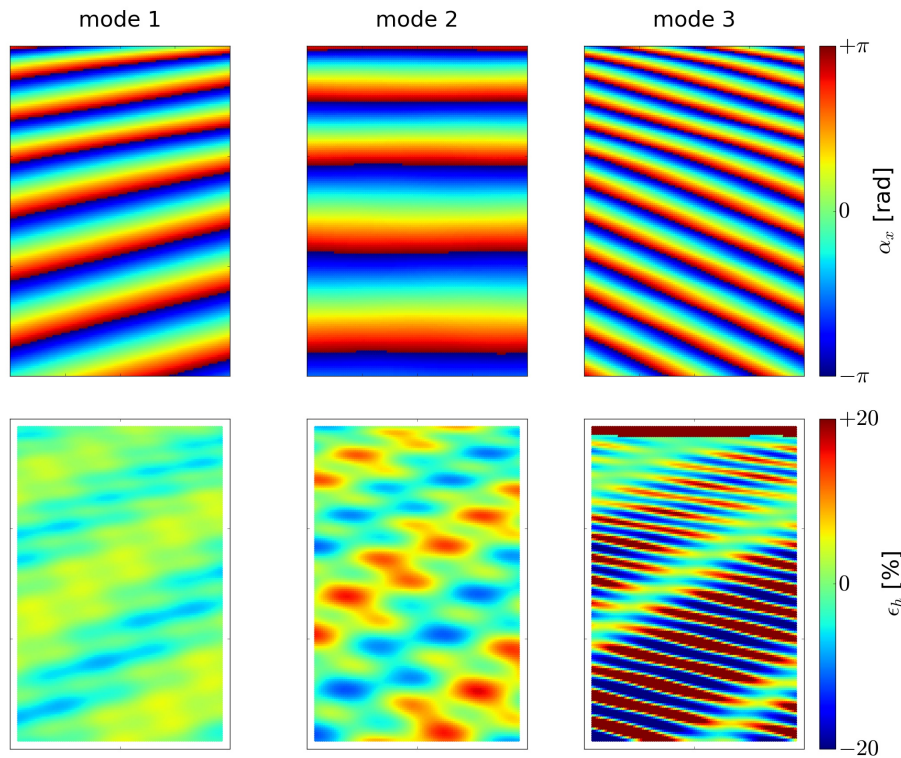


Figure 9. Phase fitting without windowing of the linear polychromatic wave field WS for $\Delta t = 0.5$ s, $\Delta x = 2$ m, $R_t = 1$ s, $R_x = 8$ m. From top to bottom: α_x and ϵ_h .

300 The PCA of the linear polychromatic wave field (WS in Figure 6) has been performed only for
 301 the default values $\Delta t = 0.5$ s, $\Delta x = 2.0$ m, $R_t = 1.0$ s and $R_x = 8$ m, so as to explore the ability of the
 302 method to identify the different wave components and to infer the bathymetry from each one of them.
 303 In this case three main modes are obtained, see Table 6 (lower half), that accumulate a 99.2 % of the
 304 variance. The periods of each of these modes coincide with those of the corresponding constitutive
 305 linear waves. Further, the variance of each of them corresponds to the one predicted by equation (6)
 306 from each of the amplitudes (which are 71.1 %, 25.7 % and 2.8 %). The angle α_x of these three modes
 307 (Figure 9, upper panels), reproduce well each respective linear wave train. A summary of the errors in
 308 k and h is included in Table 6 (lower half). The errors in k and h increase with the mode number and,
 309 again, the largest errors in h occur for the third mode, which corresponds to the smallest period (W3).
 310 However, the bathymetry can be successfully retrieved from the first mode, with a relative error of
 311 only 3 %.

312 3.2. Analysis for synthetic nonlinear waves: function fitting and windowing

313 Nonlinear wave propagation over a nonuniform bathymetry has also been analyzed. The goal is
 314 to test the capability of the new bathymetry inversion method under more challenging conditions and
 315 to gain a better understanding of function fitting and windowing methods. The proposed bathymetry
 316 is based on the one for linear waves, but with the addition of three sand banks: two in the region
 317 of the bar, simulating a crescentic bar, and another one near the shore, simulating a transverse bar
 318 (Figure 5, right). Nonlinear waves are modelled with the fully nonlinear Boussinesq-type model
 319 FUNWAVE [36] (see Appendix A for details). Unlike in the linear propagation model used above,
 320 wave reflection is allowed to happen in FUNWAVE. Only two wave fields are considered in this
 321 section: W1 (monochromatic) and WS (polychromatic). The influence of the wave height is analyzed
 322 through three multiplying factors for the wave amplitudes in Table 3 (which now represents the
 323 real wave amplitudes). The three multiplying factors are $F = 1.0$ as reference case, $F = 0.25$ for

factor F	mode	σ^2 [%]	T [s]
0.25	1	98.7	7.953 [W1]
1.0	1	94.6	7.948 [W1]
	2	3.9	3.961 [—]
2.5	1	87.6	7.955 [W1]
	2	8.4	3.958 [—]
	3	2.0	2.637 [—]

Table 7. Results of the PCA obtained for nonlinear wave propagation of the monochromatic W1 case with different F factors. Next to the retrieved period, the corresponding wave field is indicated (when applicable).

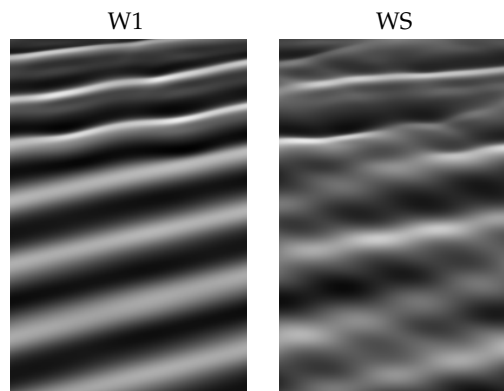


Figure 10. Initial snapshots for synthetic nonlinear wave trains W1 and WS for $F = 2.5$. Spatial domain is $200 \text{ m} \times 300 \text{ m}$ (in the alongshore and cross-shore directions, respectively) and pixel intensity is a linear function of the modelled free surface elevation.

324 smaller nonlinearities (i.e., wave amplitudes $A_1 = 2.5 \text{ cm}$, $A_2 = 1.5 \text{ cm}$ and $A_3 = 0.5 \text{ cm}$), and $F = 2.5$
 325 ($A_1 = 25.0 \text{ cm}$, $A_2 = 15.0 \text{ cm}$ and $A_3 = 5.0 \text{ cm}$). Figure 10 shows snapshots of the wave fields. In the
 326 forthcoming analysis, $\Delta t = 0.532 \text{ s}$, $\Delta x = 2.0 \text{ m}$, $R_t = 1.1 \text{ s}$ and $R_x = 8 \text{ m}$.

327 The computations for the first wave field case, W1, are presented to show how the nonlinear
 328 nature of the waves is revealed in the PCA and the corresponding EOFs (Table 7). The first mode
 329 for $F = 2.5$ corresponds to the wave field W1 (period $T \approx 7.95 \text{ s}$), the second one has half the period
 330 and reflects the nonlinear transfer of the dominant wave field W1 into its first harmonic (of twice the
 331 frequency of the main one). Further on this, the third EOF has a period which is $1/3$ of that of the
 332 dominant wave field. As wave amplitudes decrease, contributions to higher harmonics are reduced
 333 and for $F = 0.25$ this nonlinear transfer is so small that only one EOF is obtained.

334 For the polychromatic wave field, WS, the complete analysis is performed and the results obtained
 335 using phase and function fitting are summarized in Table 8. For $F = 0.25$, the three modes retrieve
 336 the three wave fields W1, W2 and W3 (compare the periods in Table 8 with the ones in Table 3). For
 337 $F = 1.0$ and $F = 2.5$ the modes retrieve only W1 and W2. The first mode provides better results in
 338 all cases and function fitting method improves the results for $F = 0.25$ and $F = 1.0$. The upper half
 339 of Figure 11 shows, for $F = 1.0$, how the first two modes correspond to the first two components of
 340 the wave field (W1 and W2) while the third one seems to mix characteristics from a harmonic of W1
 341 with W3 (given that $T_1/2 \approx T_3$). Figure 11 also includes the bathymetry obtained using phase fitting.
 342 Again, as in the linear case, the bathymetries retrieved by modes 2 and 3 have larger errors than that
 343 corresponding to mode 1, and thereby only the first mode will be considered for windowing.

344 The results obtained by windowing the polychromatic case WS are shown in Table 9. The three
 345 multiplying factors F , two video lengths ($t_{\max} = 90 \text{ s}$, as above, and $t_{\max} = 150 \text{ s}$) and five different
 346 values of w_t are considered. The number of sub-videos, that is a function of t_{\max} and w_t for given
 347 Δt , are included in Table 9 in parentheses. The results have been obtained for $R'_x = R_x = 8 \text{ m}$, thus

factor F	mode	σ^2 [%]	T [s]	ϵ_h^{RMS} [%]	
				p	f
0.25	1	58.6	7.954 [W1]	19.0	10.1
	2	36.2	11.882 [W2]	54.5	23.4
	3	3.1	5.023 [W3]	24.8	10.7
1.0	1	52.5	7.951 [W1]	13.5	11.7
	2	34.2	11.870 [W2]	37.1	25.2
	3	4.2	4.779 [—]	—	—
2.5	1	45.4	7.964 [W1]	30.3	31.7
	2	31.6	11.849 [W2]	36.4	39.0
	3	6.9	4.788 [—]	—	—

Table 8. Summary of the results for nonlinear wave propagation of the polychromatic WS case with different F factors. Relative RMSE, ϵ_h^{RMS} , are given for $h \geq 0.75$ m. Here, “ p ” and “ f ” stand for phase and function fitting of the wavenumber. Next to the retrieved period, the corresponding wave field is indicated (when applicable).

348 introducing some spatial filtering. The results for $R'_x = 0$ have larger errors ($\sim 50\%$ higher, not shown).
 349 Applying windowing method improves the results of phase fitting method (for certain optimal values
 350 of w_t) and the obtained relative RMSE in h can remain below 15% for the three values of F.

351 As an example, Figure 12 shows, for the three inversion methods, the relative errors, ϵ_h , obtained
 352 for $F = 1.0$, $t_{\text{max}} = 150$ s (and using $w_t = 60$ s for windowing). In this case, both function fitting and
 353 windowing improve the result of phase fitting in all the domain. However, as in the 1D example, at
 354 function fitting method shows, at some points, peaks due to an optimization failing.

t_{max}	F	ϵ_h^{RMS} [%]						
		p	f	windowing, w_t [s]				
				30	40	60	80	90
90 s	0.25	19.0	10.1	(112)	(94)	(56)	(18)	(1)
	1.00	13.5	11.7	28.0	13.1	13.6	16.2	19.0
	2.50	30.3	31.7	28.1	10.3	10.8	14.1	13.5
150 s	0.25	18.4	8.2	(225)	(207)	(169)	(131)	(113)
	1.00	13.0	10.1	24.8	11.6	12.0	11.9	11.0
	2.50	27.5	26.5	24.2	8.2	8.8	8.6	7.0
				99.1	52.5	43.2	30.9	15.1

Table 9. Results for the first mode for nonlinear wave propagation of the polychromatic WS case with different F factors, total video length t_{max} , and window width w_t . Relative RMSE, ϵ_h^{RMS} , are given for $h \geq 0.75$ m. Here, “ p ” and “ f ” stand for results using phase and function fitting for t_{max} , respectively. The number of sub-videos are included in parentheses.

355 4. Discussion

356 4.1. Error sources

357 As already seen in the 1D linear example (Figure 3 monochromatic and bi-chromatic cases), while
 358 the errors in k are similar both in deep and shallow waters (they are almost negligible in the first mode),
 359 the errors in h are much larger in the deeper region. This is a consequence of how the errors, both in ω
 360 and in k , propagate to the inverted water depth. Recalling the dispersion relationship, we can write

$$|\epsilon_h| \leq |\delta_\omega \epsilon_\omega| + |\delta_k \epsilon_k|,$$

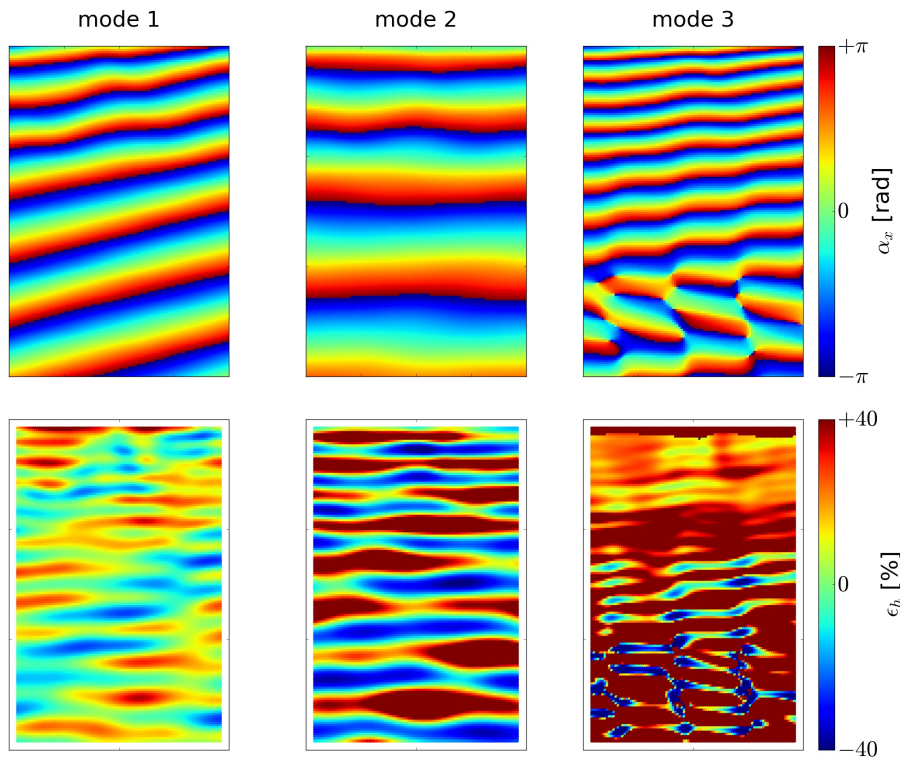


Figure 11. Results for α_x (top) and ϵ_h (bottom) obtained with the phase fitting method without windowing from the nonlinear polychromatic wave field WS with $F = 1.0$ for $\Delta t = 0.532$ s, $\Delta x = 2$ m, $R_t = 1.1$ s, $R_x = 8$ m and $t_{\max} = 90$ s.

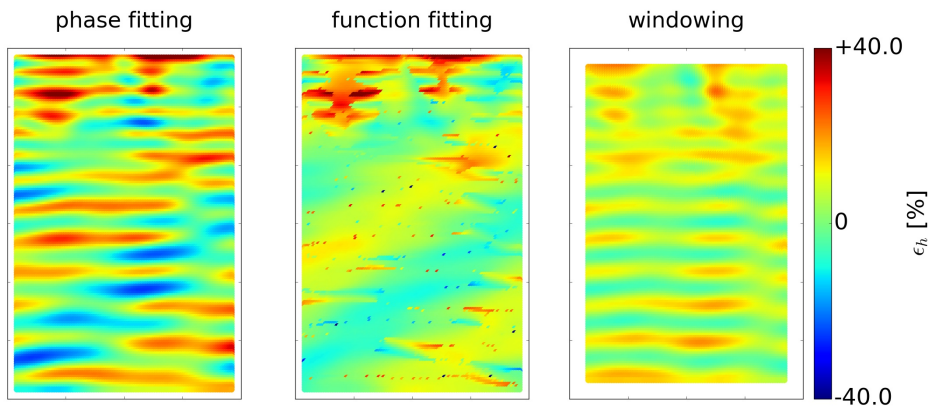


Figure 12. Results for ϵ_h obtained with phase fitting, function fitting and windowing (with $w_t = 60$ s) from the first mode for the nonlinear polychromatic wave field WS with $F = 1.0$, $\Delta t = 0.532$ s, $\Delta x = 2$ m, $R_t = 1.1$ s, $R_x = 8$ m and $t_{\max} = 150$ s.

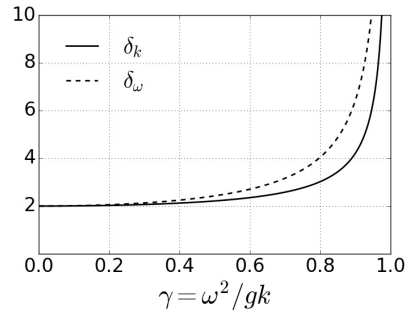


Figure 13. Propagation of the errors in k and ω to water depth h when using the dispersion relation.

361 for the relative errors ϵ_h , ϵ_ω and ϵ_k , with

$$\delta_\omega = \frac{\omega}{h} \frac{dh}{d\omega} = \frac{2\gamma}{(1-\gamma^2)\operatorname{atanh}(\gamma)}, \quad \delta_k = \frac{k}{h} \frac{dh}{dk} = \frac{1}{2}\delta_\omega + 1.$$

362 Here, $\gamma = \omega^2/gk$. Figure 13 shows δ_k and δ_ω as functions of γ . This figure is similar to that by [11]
 363 for δ_k , but here including δ_ω . For $\gamma \gtrsim 0.8$ (which is equivalent to $kh \gtrsim 1.10$ or $\omega^2 h/g \gtrsim 0.88$), the
 364 propagation errors are large and increase rapidly. The physical reason is that waves do not feel the
 365 bottom if water depth is much larger than their wavelength.

366 Note that the number γ increases both if the water depth increases or the wave period diminishes.
 367 A critical analysis of the results in the view of the values of γ is crucial. In the 1D linear example shown
 368 in Section 2.4, γ goes from 0.53 in the shallow area to 0.93 in the deeper area, with the corresponding
 369 observed amplification of the errors in h (Figure 3). In the 2D examples, the bathymetry retrieved from
 370 W3 gives the largest errors (e.g., Table 6) because the period is the smallest ($T = 5.0$ s) and $\gamma \gtrsim 0.8$ for
 371 $h \gtrsim 5.5$ m, i.e., inside the studied domain (for W1, $T = 7.95$ s, so that $\gamma \gtrsim 0.8$ for $h \gtrsim 13.5$ m, outside
 372 the studied domain).

373 4.2. Sensitivity to Δt , Δx , R_t and R_x

374 The influence of the spatio-temporal discretization of the signal has been analyzed through the
 375 linear propagation of W1. One major result of the PCA for monochromatic waves is to obtain one main
 376 mode that explains more than 98%. The error of the wave frequency, ϵ_ω , depends mainly on Δt and R_t
 377 (not on Δx). The radius R_t (that has to be $\geq \Delta t$) is required to be smaller than $T/2$ (Table 4) to avoid
 378 the jumps of \hat{a}_t , i.e., it has to hold $\Delta t \leq R_t < T/2$. Once this condition is satisfied, the errors in ω are
 379 small in all cases. Similarly, for the recovery of k through phase fitting Δt plays a minor role and the
 380 condition $\Delta x \leq R_x < L/2$ must hold, where L is the wavelength (which will depend on h for a given
 381 ω). In this case, the error ϵ_k^{RMS} reduces as Δx and R_x reduce (Table 5), getting stable for $\Delta x \leq 4$ m and
 382 $R_x \leq 8$ m (the wavelength in that case ranged from ~ 20 m to ~ 65 m).

383 4.3. Sensitivity to the inversion method, t_{\max} and w_t

384 While phase fitting is the only alternative proposed for the recovery of ω from PCs, three different
 385 approaches are considered to recover k from the EOFs: phase fitting, function fitting and windowing.
 386 Windowing for k relies on phase fitting, applying windowing on function fitting has been disregarded
 387 due to the high computational cost.

388 Function fitting turns out to be the best choice whenever wave reflection is not negligible or there
 389 are two wave fields with the same frequency (e.g., Figure 3, function fitting panels). Windowing is
 390 able, in general, to reduce the oscillatory patterns of phase fitting, but it does not work for cases with
 391 non negligible reflection (e.g., Figure 3, windowing panels). Regarding the more realistic nonlinear 2D
 392 wave fields, windowing with a convenient w_t can reduce the errors compared to both phase fitting
 393 (p) and even function fitting (f) for F in $\{1.0, 2.5\}$ (Table 9). For $F = 0.25$ windowing can improve

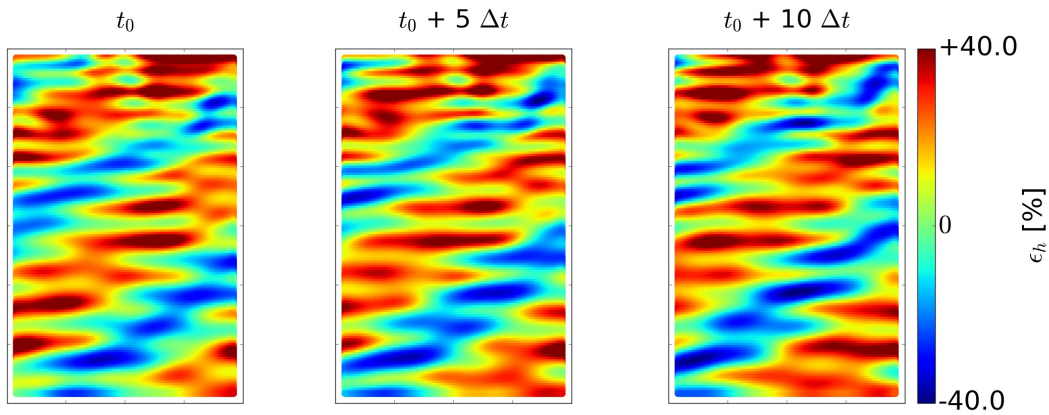


Figure 14. Propagation of the errors ϵ_h in the bathymetry inversion for three time windows.

394 the phase fitting results (likely removing part of the oscillatory patterns), but not those of function
 395 fitting. Actually, wave reflection, though small, is not negligible for $F = 0.25$. In that case there is little
 396 wave breaking, less energy dissipation and, therefore, more wave reflection. Wave reflections are in
 397 general small in dissipative beaches, but may play a role in reflective beaches (e.g., beaches with large
 398 slopes or short waves) or in areas with structures such as harbours. Whenever wave reflection is not
 399 negligible, function fitting should be considered.

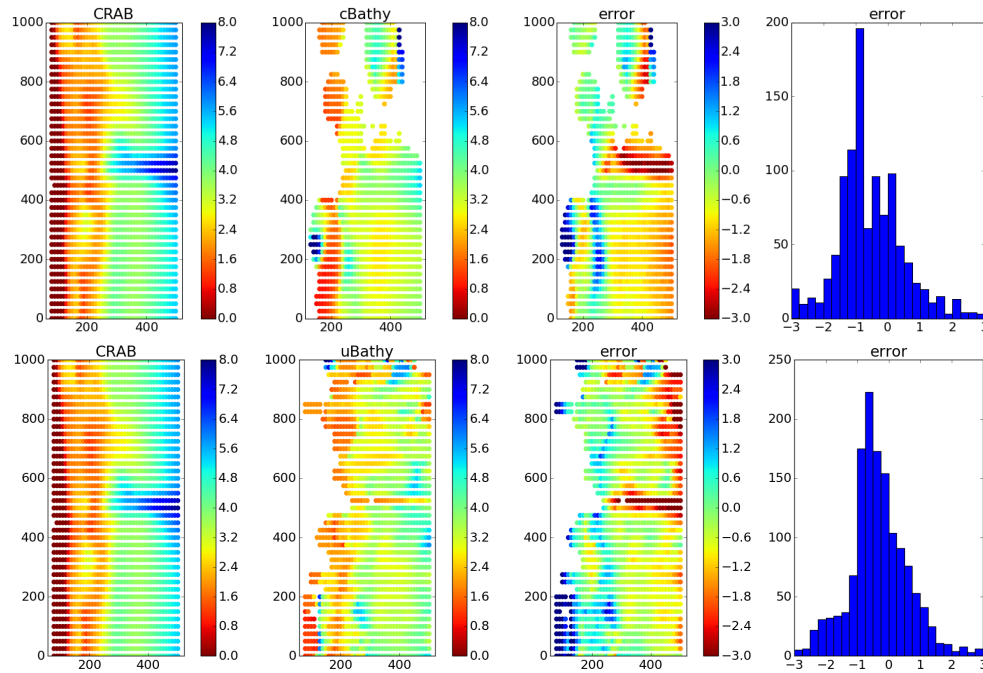
400 Figure 14 shows how windowing mitigates oscillatory patterns. The figure shows the relative
 401 errors of h recovered from three different sub-videos. The oscillatory pattern of the error propagates
 402 similar to the own wave field component. Therefore, provided that there are sufficient sub-videos,
 403 the errors are compensated to some extent in the averaging process. The more sub-videos there are
 404 available, the better the windowing will filter the oscillatory pattern, as long as the quality of the ω and
 405 h recovered from each sub-video are *sufficiently* good. This fact can be seen in the Table 9 (especially for
 406 $F = 1.0$). For small values of w_t the error is greater than that obtained for the analysis of the complete
 407 video (t_{\max} duration), however as w_t increases the error diminishes. For excessively large values of w_t
 408 the error rises again as the number of sub-videos is reduced. The dependency on w_t becomes stronger
 409 for increasing F (more nonlinear waves).

410 4.4. Field data

411 The present methodology has finally been applied to a video from a real field site in which waves
 412 are not only nonlinear but also affected by noise. The results have been compared to those obtained
 413 from cBathy. The cBathy code and the wave video snaps for test have been obtained from the GitHub
 414 distribution [37], managed by the Coastal Imaging Research Network. The cBathy code and images
 415 used (October 22, 2011 at 15h in Duck, NC) are part of the study presented by [12]. The video consists
 416 of 2048 snaps at 2 Hz. The spatial domain of the video covers a region of $1000 \text{ m} \times 500 \text{ m}$ with an
 417 irregular mesh of 8576 points (the spatial mesh not being regular does not make a difference for the
 418 present approach). The dominant wave period is around $T \sim 15 \text{ s}$, the wavelengths are around 100 m,
 419 and wave breaking was present in some regions of the domain (lower left part). The ground truth
 420 was obtained through a Coastal Research Amphibious Buggy (CRAB) on October 19, 2011, and the
 421 results are known in a regular mesh (Figure 15), so that all the results from the video analysis were
 422 interpolated to the CRAB mesh for comparison purposes. The reader is referred to the work by [12]
 423 for further details on the data set.

424 The video, of around 16 minutes, has been analyzed using the windowing method with $w_t = 80 \text{ s}$
 425 (i.e., around 5 periods). The results without windowing were unsatisfactory (not shown). For each
 426 sub-video only the dominant mode is considered. Also, $R_t = 1.5 \text{ s}$ (for frequency recovery) and, given
 427 the long wavelengths, $R'_x = R_x = 30 \text{ m}$ (for wavenumber recovery). Regarding cBathy, the code is

	cBathy	uBathy
percentage of points	60 %	84 %
average error (bias)	-0.50 m	-0.27 m
RMS error	1.38 m	1.29 m

Table 10. Summary of the results for the field site video analysis.**Figure 15.** On top (bottom) results from cBathy (uBathy). From left to right: measured bathymetry with the CRAB, inferred bathymetry, error of the inferred bathymetry (in m), and histogram of the errors for the pixels.

428 applied without modifying any parameter and the Kalman filter is not used (since we consider only
 429 one video). The results obtained both from cBathy and the new methodology (“uBathy”) are shown in
 430 Figure 15, together with the ground truth bathymetry provided by the “CRAB” (the plot is doubled for
 431 ease). In regions with observed wave breaking, where the dispersion relation is not applicable, the
 432 errors increase with both methodologies. As shown in Table 10, uBathy improves the results obtained
 433 with cBathy. It not only recovers a higher amount of points (40 % more) but also provides smaller
 434 average error (bias) and RMSE. This proves that the new proposed methodology is also valid to handle
 435 the noisy wave conditions occurring in real beaches. The computational times to analyse the video
 436 with “cBathy” and “uBathy” were of the same order of magnitude.

437 4.5. Future work

438 Several known issues require further analysis or remain still open. Such issues will be investigated
 439 in the future by applying systematically the present approach to real field site videos. First, the
 440 wavelength depends on h and, therefore the values of R_x (and R'_x) could be a function of a previous
 441 estimate (if available) of the bathymetry. Second, when using real videos there will be the possibility
 442 that some regions of the wave field are particularly noisy at given time intervals (e.g., due to passing
 443 of moving objects). This suggests the extension of the (time) windowing scheme proposed above to a
 444 space-time windowing scheme. Third, the window width w_t can be chosen as a function of the wave
 445 period T (namely, $w_t \propto T$). The exact length of each sub-video is relevant for the quality of its result,
 446 according to Figure 4 (in that figure, t_{\max} plays the role of w_t , since there is just one video). By properly

447 choosing the windows width the errors could probably be reduced. Fourth, when dealing with a series
448 of hourly videos, following [15], a Kalman filter should be used.

449 Finally, for real field site wave conditions, it is recommendable to retrieve the bathymetry for
450 adequate conditions: monochromatic waves of small height (ideally), with an adequate wave period
451 for the desired depths to be measured. In case of macro-tidal conditions, the method can be applied
452 both in high tide (to obtain the bathymetry of the shallower area) and in low tide (to obtain the deeper
453 area bathymetry). In dissipative beaches, where wave reflection is minor, the method using phase
454 fitting with windowing should provide better results, whilst in reflective beaches, function fitting
455 method should be applied.

456 5. Conclusions

457 A new methodology to retrieve the bathymetry out of wave propagation recorded by coastal
458 video monitoring systems has been presented. It is based on Principal Component Analysis (PCA) of
459 the Hilbert transform of video images. The method is first tested and validated with synthetic wave
460 fields over known bathymetries. A first set of examples of wave fields are obtained with linear wave
461 theory, which describes the propagation of waves of infinitesimal height over an alongshore uniform
462 bathymetry. To generate more realistic conditions, a fully nonlinear Boussinesq-type model is also
463 applied to propagate finite-amplitude waves over a more complex alongshore variable bathymetry.
464 Finally, a field site video is also used to test the method under real wave conditions. A major result of
465 the present contribution is that PCA successfully provides a decomposition of the videos into a set
466 of modes associated to the different components of the wave propagation field, even when waves
467 have large amplitudes (i.e., large nonlinearities). In the latter case, the PCA also allows to isolate the
468 subharmonic components.

469 The frequency (ω) of the wave trains are obtained by *phase fitting* the angles of the PCs, which
470 successfully works in all the studied conditions. Three different approaches have been developed
471 to obtain the wavenumber (k). Performing a *phase fitting* of the angles of the Empirical Orthogonal
472 Functions (EOFs) can only resolve well the linear wave cases but it fails under more realistic conditions.
473 Making a *function fitting* of the angles of the EOFs, enables to accurately obtain the wavenumbers in
474 most of the tested conditions and it can even identify incident and reflected constituents, but it has a
475 high computational cost. Applying a time *windowing* to the phase-fitting method greatly improves the
476 results and provides accurate values of the bathymetry for all tested cases, being much more efficient
477 computationally, but it fails when there are reflected waves. The latter is the recommended method to
478 use in dissipative beaches but in sites with significant wave reflection the function fitting method is
479 the only valid approach.

480 Once ω and k are obtained, the local water depth is successfully estimated by inverting the wave
481 dispersion relation (for water depths $0.75 \text{ m} \leq h \leq 8.0 \text{ m}$), after establishing the optimal values for
482 all the parameters. When the methodology is applied to a field of monochromatic or polychromatic
483 linear waves on the alongshore-uniform bathymetry, relative errors in h do not exceed 3.5% (using
484 the phase-fitting method for k). For the more realistic case of polychromatic nonlinear waves over a
485 complex bathymetry, the relative root-mean-square errors in h are around 15% (using the windowing
486 method for k). An application to a real video obtained in a field site confirms the capability of the
487 present methodology to handle realistic wave conditions. Compared to a state-of-the-art bathymetry
488 extraction code, the present new approach recovers a 40% larger amount of points and the overall
489 error is smaller.

490 **Author Contributions:** The first two authors have equally contributed to the work. Conceptualization, G.S. and
491 D.C.; methodology, G.S., D.C. and P.L.; software, G.S.; validation, G.S., D.C. and P.L.; formal analysis, G.S., D.C.,
492 P.L., A.O. and F.R.; investigation, G.S., D.C., P.L., A.O. and F.R.; resources, G.S., D.C. and P.L.; writing—original
493 draft preparation, G.S. and D.C.; writing—review and editing, G.S., D.C., A.O. and F.R.; visualization, G.S., D.C. and
494 P.L.; supervision, G.S., D.C.; project administration, G.S. and D.C.; funding acquisition, G.S., D.C., A.O. and F.R.

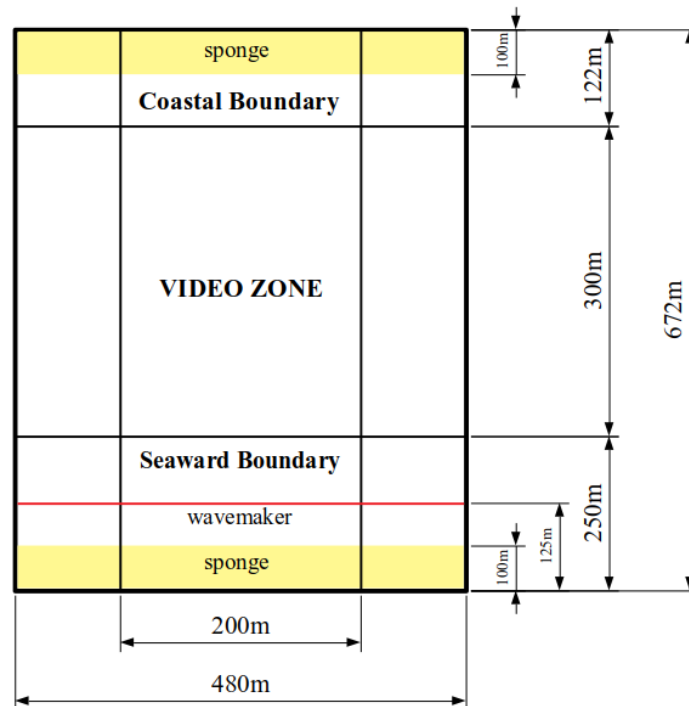


Figure A1. Domain used in the FUNWAVE simulations, where the study region is called video zone.

495 **Funding:** This research was funded by the Spanish Government (MINECO/MICINN/FEDER) grant
 496 numbers CTM2015-66225-C2-1-P and CTM2015-66225-C2-2-P, RTI2018-093941-B-C31, RTI2018-093941-B-C32
 497 and RTI2018-093941-B-C33

498 **Acknowledgments:** The authors would like to thank Prof. Dr. R. A. Holman for providing the cBathy code and
 499 for the stimulating discussions. The authors also acknowledge the useful suggestions from E. Abella.

500 Abbreviations

501 The following abbreviations are used in this manuscript:

CRAB Coastal Research Amphibious Buggy
 CSM Cross Spectral Matrix
 PCA Principal Component Analysis
 502 EOF Empirical Orthogonal Function
 PC Principal Component
 RMSE Root Mean Square Error

503 Appendix A. Nonlinear wave field generation

504 To model nonlinear waves, FUNWAVE-TVD [36] has been used, which simulates wave
 505 propagation over a rectangular domain employing a set of fully-nonlinear Boussinesq equations.
 506 The wave forcing input is modelled by a source term in the equations (the wavemaker), localized in
 507 some internal region of the domain. It needs to be placed over a constant depth, and must have a
 508 thickness comparable to the wavelengths present in the domain (usually > 0.25 wavelengths). The
 509 wavemaker used is called WK_DATA2D and adds up monochromatic waves of frequency, orientation
 510 and amplitude specified by the user. The source code has been modified to also accept the phases of the
 511 monochromatic waves (originally, it used random ones). The coastal and the offshore boundaries are
 512 modelled with sponges followed by reflective walls. Direct sponges have been used, which attenuate
 513 the value of variables over the sponged cells. The values used for the parameters verify that the sponge
 514 thickness is of the order of the wavelength and that most of wave energy is absorbed. In the laterals,
 515 periodic boundary conditions are implemented.

516 The bathymetry shown in Figure 5 (right panel) is implemented here in the so-called video zone,
517 which has dimensions of 200 m × 300 m (alongshore and cross-shore, respectively) as in the linear
518 wave case. However, the FUNWAVE domain has been extended to fit the wavemaker and the sponges
519 (Figure A1). Instead of the original seaward depth limit of 7.3 m, the profile is extended up to 8 m depth,
520 and then becomes constant. For the frequencies used, this depth results in a maximum wavelength
521 of about 100 m. Therefore, the thickness of the wavemaker is 25 m, and that of the sponges is 100 m.
522 The extension in the offshore boundary is of 250 m to fit the wavemaker, the sponge and separation
523 spaces for safety. A coastal extension of 122 m that includes a sponge is also implemented. In order
524 to limit reflection and to avoid breaking the bathymetry is clipped to 0.3 m there. However, some
525 wave reflection still occurs, although the reflected wave has a tiny amplitude. In the laterals, a space
526 of 140 m at each side is used to minimize potential influences of the periodic boundary conditions
527 into the domain (Figure A1). The grid size is of 1 m both in cross-shore and in alongshore directions.
528 The first 200 s are the warm-up time and the subsequent 150 s become the videos used for bathymetry
529 inversion.

530 References

- 531 1. Davidson, M.; Van Koningsveld, M.; de Kruif, A.; Rawson, J.; Holman, R.; Lamberti, A.; Medina, R.; Kroon,
532 A.; Aarninkhof, S. The CoastView project: Developing video-derived Coastal State Indicators in support of
533 coastal zone management. *Coastal Engineering* **2007**, *54*, 463–475. doi:10.1016/j.coastaleng.2007.01.007.
- 534 2. Kroon, A.; Davidson, M.; Aarninkhof, S.; Archetti, R.; Armaroli, C.; Gonzalez, M.; Medri, S.; Osorio,
535 A.; Aagaard, T.; Holman, R.; Spanhoff, R. Application of remote sensing video systems to coastline
536 management problems. *Coastal Engineering* **2007**, *54*, 493–505. doi:10.1016/j.coastaleng.2007.01.004.
- 537 3. Calvete, D.; Coco, G.; Falqués, A.; Dodd, N. (Un)predictability in rip channel systems. *Geophysical Research*
538 *Letters* **2007**, *34*. doi:10.1029/2006GL028162.
- 539 4. Arriaga, J.; Rutten, J.; Ribas, F.; Falqués, A.; Ruessink, G. Modeling the long-term diffusion and feeding
540 capability of a mega-nourishment. *Coastal Engineering* **2017**, *121*, 1–13. doi:10.1016/j.coastaleng.2016.11.011.
- 541 5. Birkemeier, W.; Mason, C. The crab: A unique nearshore surveying vehicle. *Journal of Surveying Engineering*
542 **1984**, *110*, 1–7. doi:10.1061/(ASCE)0733-9453(1984)110:1(1).
- 543 6. Monteys, X.; Harris, P.; Caloca, S.; Cahalane, C. Spatial prediction of coastal bathymetry based
544 on multispectral satellite imagery and multibeam data. *Remote Sensing* **2015**, *7*, 13782–13806.
545 doi:10.3390/rs71013782.
- 546 7. Clarke, J.; Mayer, L.; Wells, D. Shallow-water imaging multibeam sonars: A new tool for investigating
547 seafloor processes in the coastal zone and on the continental shelf. *Marine Geophysical Research* **1996**,
548 *18*, 607–629. doi:10.1007/BF00313877.
- 549 8. Guenther, G.; Thomas, R.; LaRocque, P. Design considerations for achieving high accuracy with the
550 SHOALS bathymetric lidar system. 1996, Vol. 2964, pp. 54–71. doi:10.1117/12.258353.
- 551 9. Levoy, F.; Anthony, E.; Monfort, O.; Robin, N.; Bretel, P. Formation and migration of transverse bars
552 along a tidal sandy coast deduced from multi-temporal Lidar datasets. *Marine Geology* **2013**, *342*, 39–52.
553 doi:10.1016/j.margeo.2013.06.007.
- 554 10. Stumpf, R.; Holderied, K.; Sinclair, M. Determination of water depth with high-resolution satellite imagery
555 over variable bottom types. *Limnology and Oceanography* **2003**, *48*, 547–556.
- 556 11. Stockdon, H.; Holman, R. Estimation of wave phase speed and nearshore bathymetry from video imagery.
557 *Journal of Geophysical Research: Oceans* **2000**, *105*, 22015–22033.
- 558 12. Holman, R.; Plant, N.; Holland, T. CBathy: A robust algorithm for estimating nearshore bathymetry.
559 *Journal of Geophysical Research: Oceans* **2013**, *118*, 2595–2609. doi:10.1002/jgrc.20199.
- 560 13. Bell, P.S. Shallow water bathymetry derived from an analysis of X-band marine radar images of waves.
561 *Coastal Engineering* **1999**, *37*, 513 – 527.
- 562 14. Borge, J.; Rodríguez Rodríguez, G.; Hessner, K.; González, P. Inversion of marine radar images for surface
563 wave analysis. *Journal of Atmospheric and Oceanic Technology* **2004**, *21*, 1291–1300.
- 564 15. Holman, R.; Haller, M. Remote sensing of the nearshore. *Annual Review of Marine Science* **2013**, *5*, 95–113.

- 565 16. Holland, K.; Holman, R.; Lippmann, T.; Stanley, J.; Plant, N. Practical use of video imagery in nearshore
566 oceanographic field studies. *IEEE Journal of Oceanic Engineering* **1997**, *22*, 81–91. doi:10.1109/48.557542.
- 567 17. Holman, R.; Stanley, J. The history and technical capabilities of Argus. *Coastal Engineering* **2007**, *54*, 477–491.
568 doi:10.1016/j.coastaleng.2007.01.003.
- 569 18. Nieto, M.A.; Garau, B.; Balle, S.; Simarro, G.; Zarruk, G.A.; Ortiz, A.; Tintore, J.; Alvarez-Ellacuria, A.;
570 Gomez-Pujol, L.; Orfila, A. An open source, low cost video-based coastal monitoring system. *Earth Surface*
571 *Processes and Landforms* **2010**, *35*, 1712–1719. doi:10.1002/esp.2025.
- 572 19. Boak, E.; Turner, I. Shoreline definition and detection: A review. *Journal of Coastal Research* **2005**, *21*, 688–703.
573 doi:10.2112/03-0071.1.
- 574 20. Simarro, G.; Bryan, K.; Guedes, R.; Sancho, A.; Guillén, J.; Coco, G. On the use of variance images for
575 runup and shoreline detection. *Coastal Engineering* **2015**, *99*, 136–147. doi:10.1016/j.coastaleng.2015.03.002.
- 576 21. Plant, N.; Holman, R. Intertidal beach profile estimation using video images. *Marine Geology* **1997**, *140*, 1–24.
577 doi:10.1016/S0025-3227(97)00019-4.
- 578 22. Aarninkhof, S.; Turner, I.; Dronkers, T.; Caljouw, M.; Nipius, L. A video-based technique for mapping
579 intertidal beach bathymetry. *Coastal Engineering* **2003**, *49*, 275–289. doi:10.1016/S0378-3839(03)00064-4.
- 580 23. Alexander, P.; Holman, R. Quantification of nearshore morphology based on video imaging. *Marine*
581 *Geology* **2004**, *208*, 101–111. doi:10.1016/j.margeo.2004.04.017.
- 582 24. Almar, R.; Coco, G.; Bryan, K.; Huntley, D.; Short, A.; Senechal, N. Video observations of beach cusp
583 morphodynamics. *Marine Geology* **2008**, *254*, 216–223. doi:10.1016/j.margeo.2008.05.008.
- 584 25. Ojeda, E.; Guillén, J. Shoreline dynamics and beach rotation of artificial embayed beaches. *Marine Geology*
585 **2008**, *253*, 51–62. doi:10.1016/j.margeo.2008.03.010.
- 586 26. Morales-Márquez, V.; Orfila, A.; Simarro, G.; Gómez-Pujol, L.; Álvarez-Ellacuría, A.; Conti, D.;
587 Galán, A.; Osorio, A.F.; Marcos, M. Numerical and remote techniques for operational beach
588 management under storm group forcing. *Natural Hazards and Earth System Sciences* **2018**, *18*, 3211–3223.
589 doi:10.5194/nhess-18-3211-2018.
- 590 27. van Dongeren, A.; Plant, N.; Cohen, A.; Roelvink, D.; Haller, M.; Catalán, P. Beach Wizard: Nearshore
591 bathymetry estimation through assimilation of model computations and remote observations. *Coastal*
592 *Engineering* **2008**, *55*, 1016–1027. doi:10.1016/j.coastaleng.2008.04.011.
- 593 28. Aarninkhof, S.; Ruessink, B.; Roelvink, J. Nearshore subtidal bathymetry from time-exposure video images.
594 *Journal of Geophysical Research: Oceans* **2005**, *110*, 1–13. doi:10.1029/2004JC002791.
- 595 29. Bergsma, E.; Conley, D.; Davidson, M.; O'Hare, T. Video-based nearshore bathymetry estimation in
596 macro-tidal environments. *Marine Geology* **2016**, *374*, 31–41. doi:10.1016/j.margeo.2016.02.001.
- 597 30. Rutten, J.; De Jong, S.; Ruessink, G. Accuracy of Nearshore Bathymetry Inverted from X-Band Radar
598 and Optical Video Data. *IEEE Transactions on Geoscience and Remote Sensing* **2017**, *55*, 1106–1116.
599 doi:10.1109/TGRS.2016.2619481.
- 600 31. Kalman, R. A new approach to linear filtering and prediction problems. *Journal of Fluids Engineering,*
601 *Transactions of the ASME* **1960**, *82*, 35–45. doi:10.1115/1.3662552.
- 602 32. Brodie, K.L.; Palmsten, M.L.; Hesser, T.J.; Dickhudt, P.J.; Raubenheimer, B.; Ladner, H.; Elgar, S. Evaluation
603 of video-based linear depth inversion performance and applications using altimeters and hydrographic
604 surveys in a wide range of environmental conditions. *Coastal Engineering* **2018**, *136*, 147 – 160.
- 605 33. Merrifield, M.; Guza, T. Detecting Propagating Signals with Complex Empirical Orthogonal Functions: A
606 Cautionary Note. *Journal of Physical Oceanography* **1990**, *20*, 1628–1633.
- 607 34. Simarro, G.; Ribas, F.; Álvarez, A.; Guillén, J.; Chic, O.; Orfila, A. ULISES: An open source code for extrinsic
608 calibrations and planview generations in coastal video monitoring systems. *Journal of Coastal Research* **2017**,
609 *33*, 1217–1227. doi:10.2112/JCOASTRES-D-16-00022.1.
- 610 35. Svendsen, I.A. *Introduction to Nearshore Hydrodynamics*; 2017. doi:10.1142/5740.
- 611 36. Shi, F.; Kirby, J.; Harris, J.; Geiman, J.; Grilli, S. A high-order adaptive time-stepping TVD solver for
612 Boussinesq modeling of breaking waves and coastal inundation. *Ocean Modelling* **2012**, *43-44*, 36–51.
613 doi:10.1016/j.ocemod.2011.12.004.
- 614 37. Coastal-Imaging-Research-Network/cBathy-Toolbox. [https://github.com/Coastal-Imaging-Research-](https://github.com/Coastal-Imaging-Research-Network/cBathy-Toolbox)
615 [Network/cBathy-Toolbox](https://github.com/Coastal-Imaging-Research-Network/cBathy-Toolbox). Accessed: 2018-06-25.

616 © 2019 by the authors. Submitted to *Remote Sens.* for possible open access publication
617 under the terms and conditions of the Creative Commons Attribution (CC BY) license
618 (<http://creativecommons.org/licenses/by/4.0/>).